Electrochimica Acta 251 (2017) 1–11

Contents lists available at ScienceDirect

Electrochimica Acta

journal homepage: www.elsevier.com/locate/electacta

Research paper

Effects of low temperature annealing on the photo-electrochemical performance of tin-doped hematite photo-anodes

Franky E. Bedoya-Lora[a,*], Anna Hankin[a], Isaac Holmes-Gentle[a], Anna Regoutz[b], Manuela Nania[a], David J. Payne[b], João T. Cabral[a], Geoff H. Kelsall[a]

[a] Departments of Chemical Engineering, Imperial College London, London, SW7 2AZ, UK
[b] Departments of Chemical Engineering and Materials, Imperial College London, London, SW7 2AZ, UK

ARTICLE INFO

Article history:
Received 30 April 2017
Received in revised form 13 August 2017
Accepted 14 August 2017
Available online 19 August 2017

Keywords:
Photo-electrochemical characterisation
hematite
photo-anode
water splitting
annealing

ABSTRACT

The effects of post-deposition annealing at 400 and 500 °C on the photo-electrochemical performance of Sn^{IV}-doped α-Fe_2O_3 photo-anodes are reported. Samples were fabricated by spray pyrolysis on fluorine-doped tin oxide (FTO) and on titanium substrates. Photo-electrochemical, morphological and optical properties were determined to explain the shift in photocurrent densities to lower electrode potentials and the decrease of maximum photocurrent densities for alkaline water oxidation after annealing. Annealing at 400 and 500 °C in air did not affect significantly the morphology, crystallinity, optical absorption or spatial distributions of oxygen vacancy concentrations. However, XPS data showed a redistribution of Sn^{IV} near Sn^{IV}-doped α-Fe_2O_3 | 1 M NaOH interfaces after annealing. Thus, electron-hole recombination rates at photo-anode surfaces decreased after annealing, shifting photocurrents to lower electrode potentials. Conversely, depletion of Sn^{IV} in the α-Fe_2O_3 bulk could increase recombination rates therein and decrease photon absorption near 550 nm, due to an increased dopant concentration in the semiconductor depletion layer. This accounted for the decrease of maximum photocurrents when electron-hole recombination rates were suppressed using HO_2^- ions as a hole scavenger. The flat band potential of Sn^{IV}-doped α-Fe_2O_3 remained relatively constant at ca. 0.7 V *vs.* RHE, irrespective of annealing conditions.

1. Introduction

Solar energy harvesting using devices such as photovoltaic modules needs to be coupled to energy storage due to the diurnal and intermittent nature of solar energy. Hydrogen is a candidate for such chemical energy storage, because of its facile oxidation in fuel cells without formation of harmful by-products [1]. Splitting liquid water to produce hydrogen (and oxygen) using solar energy requires a minimum of 1.48 eV under thermoneutral conditions. Prospectively, photo-electrochemical reactors could produce hydrogen directly using solar energy, but photo-electrode materials are yet to be adequately efficient, durable, and produced by an economic fabrication process.

Hematite has been studied extensively as a possible photo-anode material for water splitting [2]. However, it requires an electrical bias to oxidise water effectively as the energy of its conduction band edge is too low and exhibits low energy conversion efficiencies. Numerous approaches for improving this material have been suggested such as doping [3], inclusion of quantum dots [4], improved synthesis pathways such as ALD [5], electrodeposition [6], and high temperature annealing [7] and reductive annealing [8]. In order to enhance the properties of photo-electrodes such as hematite, it is important to understand how the changes produced by different treatments, such as annealing, affect the properties and ultimately their performance. Post-deposition annealing of hematite thin films in air has been suggested as an essential treatment to achieve the adequate crystallinity and decrease concentrations of defects in the structure [9]. Reductive annealing [8] and hydrogen treatment [10] have also been suggested as ways to improve the photo-activity of hematite, creating oxygen deficiencies in its structure and hence improving its conductivity. Other hypotheses have also been proposed to explain the behaviour of hematite after

* Corresponding author.
E-mail address: f.bedoya-lora13@imperial.ac.uk (F.E. Bedoya-Lora).

http://dx.doi.org/10.1016/j.electacta.2017.08.090

annealing, ranging from catalytic effects to morphological changes [11].

The substrate used as support for the thin films also needs to fulfil several requirements: mechanical and chemical stability, high conductivity that would minimise in-plane ohmic losses and compatibility with photo-electrodes in terms of interfacial properties of electrical junction formed. Behaviour at elevated temperatures should also be considered when the synthesised films require heat treatment. Traditionally, hematite is deposited on conductive films such as fluorine-doped tin oxide (FTO) or indium tin oxide (ITO) on glass. These substrates are readily available and transparent, which is a useful characteristic for back-illumination. Small electrodes fabricated on these substrates do not suffer from significant ohmic losses and mechanical fragility. However, scale-up of electrodes to > 0.01 m^2 results in electrical potential losses due to relatively low conductivity [12], 8 Ω per square (FTO, TEC-8 Pilkington) and renders them more easily breakable. Sn^{IV} is also known to interact beneficially with hematite at temperatures > 600 °C [13,14], demonstrating that FTO and ITO substrates are not entirely inert. Alternatively, hematite has been synthetized on titanium foil due to its chemical stability in alkaline conditions [15] and high conductivity that serves to minimise ohmic losses. However, heat treatment in air causes growth of TiO_2 film of several nanometers [16], which could interact with hematite thin films even at 500 °C [15].

Doping of hematite photo-anodes has been suggested as a strategy to improve their electrical conductivity [17] and decrease electron-hole recombination rates in their bulk [2]. This can also be achieved by back-illumination (through the substrate) of un-doped hematite, exhibiting up to 3-fold increase of incident-to-photon current efficiency [18–20], but the high sheet resistance of the required transparent substrate limits scale-up. Conversely, back-illumination has been proved to be counterproductive for doped hematite, the electrical conductivity of which was increased and electron-hole recombination rates decreased in the bulk material, while the sluggish diffusion of holes through the film was the limiting step [21]. A 90% decrease in photocurrent was reported compared with that for front-illumination. Dopants such as Sn^{IV} have been used extensively to enhance photo-activity of hematite photo-electrodes, where Sn^{IV} acts as donor centre after replacing Fe^{III} sites [3]. Sn^{IV}-doped photo-electrodes exhibited higher donor densities of ca. 10^{26} and 10^{27} m^{-3} for doping concentrations between 0.5 and 2% mass [22]. These values are two orders of magnitude greater than for undoped hematite [10,23]. Donor densities reported here (ca. 1.3% mass Sn^{IV} doping) are as high as 10^{25} to 10^{27} m^{-3}. In this case, these unusually high values could have been affected by the concentration of oxygen vacancies in non-stoichiometric hematite Fe_2O_{3-x}, a higher electro-active area compared to geometrical area, or the presence of chloride ions at the surface [24]. Contrary to the hypothesis that doping with Sn^{IV} affects mainly bulk electron-hole recombination rates, it has been shown recently that it also affects rates of hole transfer and catalysis of the oxygen evolution reaction on hematite photo-anodes [25]. On the other hand, it has been reported that an increase in Sn^{IV} concentrations decreases the absorption of photons substantially in the visible region [3], possibly due to the formation of SnO_2, which has a higher band gap (3.5 eV) [26].

To elucidate further the effects of annealing at 400–500 °C of Sn^{IV}-doped hematite on titanium, the performance of spray pyrolysed photo-anodes was assessed as a function of several properties. The understanding of these effects could also clear the path to the improvement of existing models of photocurrent prediction in photo-electrochemical reactors. The quality of such models relies critically on the accuracy of the parameters on which they are based; special attention needs to be paid to parameters such as the flat band potential and donor density as several assumptions, often inappropriate, are made en route to their determination at nanostructured photo-electrodes [27].

2. Experimental

2.1. Photo-anode fabrication

Sn^{IV}-doped α-Fe_2O_3 photo-anodes were fabricated via spray pyrolysis [15] on TEC-8 fluorine-doped tin oxide (FTO) on glass (Hartford Glass Inc., USA) and titanium foil (0.74 mm, 99.4% Alfa Aesar). Titanium substrates (10 mm × 60 mm) were polished on an automated polishing machine (Buehler) with polishing paper grade 400, 800, 1200 and finally with aqueous dispersion of < 300 nm alumina particles. Then, substrates were degreased with acetone, immersed in 0.5 M oxalic acid overnight to minimise the oxide layer thickness, rinsed with acetone and ultra-sonicated in de-ionised water, as for FTO substrates, a few minutes prior to spray pyrolysis. The precursor solution for spray pyrolysis comprised 0.1 M $FeCl_3.6H_2O$ (99.99%, Sigma Aldrich, UK) and 6×10^{-4} M $SnCl_4$ (99.995% Sigma Aldrich, UK) dissolved in ethanol absolute (AnalaR Normapur, VWR). Sn^{IV} concentration corresponds to 1.3% doping by mass. The precursor was nebulized with a quartz spray nozzle (Meinhard, USA) at a height of 150 mm above the surface of the substrate. The nozzle movement was controlled by WinPC-NC CNC Software (BobCad-CAM, USA). The precursor solution was delivered using a syringe pump at 2 cm^3 min^{-1} and pressurised air was supplied at 345 kPa. Substrates were placed on a hotplate at 480 °C and took approximately 15 min to reach that temperature. Next, 40 passes of the nebuliser over the substrate were programmed to obtain 47 ± 6 nm thick hematite films, which was measured with a profilometer (TencorAlphastep 200 Automatic Step Profiler) in a previous study [28]; each pass took 1 minute with a resting time of 1 minute between passes, and a total time of ca. 90 min. Samples were cooled to 200 °C before being removed from the hotplate to continue cooling at room temperature.

The post-deposition annealing was done in a pre-heated oven (Elite Thermal Systems, Ltd.) at 400 and 500 °C in air at atmospheric pressure over the course of an hour. Ti|Sn^{IV}-Fe_2O_3 samples were extracted at 20, 40 and 60 minutes. All FTO|Sn^{IV}-Fe_2O_3 samples were treated for the full 60 minutes.

In order to minimise dark currents from non-illuminated electrode areas, samples were partially coated using insulating acrylic lacquer (45 kV mm^{-1}, RS component) to obtain an exposed area of 3 mm × 6 mm, corresponding to the dimensions of the incident light beam.

2.2. Photo-electrochemical characterization

Photo-electrochemical characterization was carried out using a photo-electrochemical cell of 60 cm^3 (PVC body with a quartz window). A potentiostat/galvanostat (Autolab PGSTAT 30 + Frequency Response Analysis module, Eco Chemie, Netherlands) was used to control the cell containing Sn^{IV}-Fe_2O_3 samples as working electrodes, a platinised titanium mesh (Expanded Metal Company, UK) as counter electrode and HgO|Hg as reference electrode (0.913 V *vs.* RHE and 0.109 V *vs.* SHE). 1 M NaOH was used as electrolyte solution, pH of ca. 13.6 and temperature 25 ± 2 °C. H_2O_2 (30%, AnalaR Normapur, VWR) was added in some cases as sacrificial electron donor at a concentration of 0.5 M.

Cyclic voltammograms were run typically from 0.5 to 2.0 V *vs.* RHE at 10 mV s^{-1} scan rate. Incident photon-to-current efficiencies (IPCE) were measured from 300 to 700 nm in 20 nm increments for 100 s at 1.51 and 1.71 V *vs.* RHE. Data for Mott-Schottky (MS) analysis was obtained from potentiostatic electrochemical

impedance (EIS) evaluated from 10^5 to 10^{-1} Hz (10 points per decade) at different potentials from 0.6 to 1.8 V *vs.* RHE.

Similarly, photo-electrochemical impedance spectra (PEIS) of photo-anodes were measured under high-intensity light. Following the methodology of Peter et al. [29,30], resistances corresponding to interfacial charge transfer and recombination processes were extracted after fitting to an equivalent circuit in order to calculate interfacial charge transfer efficiencies.

Flat band potentials were estimated using several methods: Mott-Schottky (MS), Gärtner-Butler and open circuit potential (OCP) under high light intensity in presence and absence of a sacrificial electron donor (H_2O_2) [31]. Donor densities were estimated from Mott-Schottky plots, assuming a relative permittivity of 38.2 ± 0.46 and a thickness of 47 ± 6 nm [28].

A Xe arc lamp (LOT-Oriel) of 300 W with Fresnel lenses was used to obtain a beam of 3 mm × 6 mm and a maximum power intensity of 3646 W m^{-2}. Intensity was varied with reflective neutral density filters ranging from 15% to 93% transmission (UQG-Optics, UK). The electrodes were irradiated directly (front-illumination) in the case of both Ti and FTO substrates. Wavelength was controlled with a monochromator/spectrograph (Omni-λ150, Zolix). The intensity of the light source was corrected by attenuation of electrolyte and quartz window across a wavelength range of 280–900 nm. A total transmission of 82% and a maximum effective intensity on the photo-electrode of 3000 W m^{-2} was estimated. Linearity in photocurrent with light intensity was confirmed experimentally, as reported and discussed in Fig. S1 in the supporting information. The light source was characterised and calibrated with a UV–vis spectrophotometer coupled to a CR2 cosine receptor (Black-Comet CXR-25, StellarNet, USA).

2.3. Optical and morphological characterization

Raman spectra were obtained from a Dispersive Renishaw 1000 confocal Raman system, 785 nm diode laser with maximum output power of 300 mW and 50 x objective (dry), and two-dimensional Peltier cooled charge-coupled device (CCD) camera as detector.

SEM images were captured using a Zeiss Sigma 300 Scanning electron microscope at 5.00 kV. Topographies of samples were determined by AFM using a Bruker Innova microscope in tapping mode at 0.1 Hz with Si tips (MPP-11100-W, Bruker), and processed with NanoScope software.

Absorption spectra of hematite films samples on FTO substrates were obtained using a Shimadzu UV-2600 UV–vis spectrophotometer with an integrating sphere and corrected by baseline subtraction assuming reflection and scattering are wavelength independent [32]. It was assumed that the optical properties measured on FTO would the same for the titanium substrate.

The surface of the thin films was characterised using XPS. The spectra were recorded on a Thermo Scientific K-Alpha$^+$ X-ray Photoelectron Spectrometer (XPS) system operating at 2×10^{-9} mbar base pressure. This system incorporates a monochromated, microfocused Al Kα X-ray source ($h\nu = 1486.6$ eV) and a 180° double focusing hemispherical analyser with a 2D detector. The X-ray source was operated a 6 mA emission current and 12 kV anode bias. Data were collected at 200 eV pass energy for survey and 20 eV pass energy for core level spectra using an X-ray spot size of 400 μm^2. A flood gun was used to minimize sample charging. All data were analysed using the Avantage software package.

3. Theoretical treatment

3.1. Mott-Schottky (MS) analysis

MS analysis of the change in semiconductor capacitance as a function of applied potential was used to determine flat band potentials and donor densities. In the absence of surface states, the capacitance of the semiconductor | electrolyte interface, $C_{interface}$, comprises contributions from the semiconductor capacitance, C_{SC}, and the capacitance of the Helmholtz layer, C_H in series:

$$\frac{1}{C_{interface}} = \frac{1}{C_{SC}} + \frac{1}{C_H} \tag{1}$$

$C_{interface}$ was evaluated from electrochemical impedance data; EIS data were fitted to a Randles electrical circuit [R(RC)] as shown in the inset of Fig. 7 in the results section. A procedure similar to that suggested by Dias and Durrant [23,33] was followed. C_{SC} was assumed to be approximately equal to $C_{interface}$ as typically $C_H \gg C_{SC}$. Also, it is known that nanostructured hematite does not comply with the assumptions of the MS model [27]. For an improved agreement between experimental data and fittings, a constant phase element (CPE) was used to estimate effective capacitance after correcting for a surface distribution of time constants due to surface roughness [34].

$$C_{SC} = Q_0^{1/n} R_s^{(1-n)/n} \tag{2}$$

Where Q_0 and n are the pseudo-capacitance and exponential term of the CPE respectively, and R_s is the electrolyte resistance. Donor density, n_0, and flat band potential, U_{FB}, were computed by linear data fitting of C_{SC}^{-2} against applied potential (U):

$$\frac{1}{C_{SC}^2} = \frac{2}{\varepsilon_0 \varepsilon_r e n_0}\left(U_{applied} - U_{FB} - \frac{k_B T}{e}\right) \tag{3}$$

Where k_B is the Boltzmann constant (1.381×10^{-23} J K^{-1}), e is the electronic charge (1.602×10^{-19}C), ε_0 and ε_r are the vacuum permittivity (8.854×10^{-12} F m^{-1}) and the relative permittivity (38.2 ± 0.46), respectively.

3.2. Photo-electrochemical impedance spectroscopy

Surface recombination rate coefficients can be measured using photo-electrochemical impedance spectroscopy (PEIS) [29]. A fraction of the total charge (holes) that reaches the surface recombines with electrons present in the conduction band close to the surface; the remaining charge is then transferred to oxidise species at the interface with the electrolyte and only the latter flux is effectively measured as current. These two processes, assuming pseudo-first order, are characterised by rate coefficients assigned to the electron-hole recombination and hole transfer processes, k_r and k_t, respectively. As detailed by Peter at al. [25,29,30], the interfacial charge transfer efficiency is defined as:

$$\eta_{surface} = \frac{k_t}{k_t + k_r} \tag{4}$$

This ratio can be estimated indirectly after fitting PEIS spectra to a two-time constant equivalent circuit R(C[R(RC)]) as shown in the inset of Fig. 6 in the results section [35]. This circuit accounts for two parallel processes which were clearly evident in impedance spectra, see also Fig. 9. As in the MS analysis, pure capacitances were replaced by CPEs to compensate for surface heterogeneities in order to improve the agreement between fitted and experimental data. The interfacial charge transfer efficiency can be then re-written in terms of fitted resistances:

$$\eta_{surface} = \frac{R_t}{R_t + R_r} \tag{5}$$

where R_t is the charge transfer resistance and R_r the recombination resistance. Impedance spectra at different applied potentials and under illumination were then analysed as described above to obtain interfacial charge transfer efficiencies, which depend on electron-hole recombination rates. These values were

fitted to an exponential equation in order to evaluate the interfacial charge transfer efficiency as a function of applied potential [28].

$$\eta_{surface} = \frac{A\exp(B \times \Delta\phi_{SC})}{1 + A\exp(B \times \Delta\phi_{SC})} \quad (6)$$

where A and B are fitted parameters, and $\Delta\phi_{SC} = U_{applied} - U_{FB}$ is the 'overpotential' for the photocurrent.

4. Results and discussion

4.1. Effect of doping

Previously, we determined that the performance of spray pyrolysed undoped hematite was clearly inferior to Sn^{IV}-doped samples [24]. Charge transfer efficiencies were measured for both materials (Fig. S2 in supporting information) and showed that the conductivity and photo-activity of the samples were improved drastically after doping, as has been reported in the literature [3,17,36]. More importantly, it has been shown that the presence of Sn^{IV} increased hole transfer rates and diminished the interfacial electron-hole recombination rates [25].

4.2. Effect of the substrate – FTO vs. Titanium

Fig. 1 compares potential dependences of dark and photo-induced current densities for Sn^{IV}-Fe_2O_3 samples on FTO and Ti substrates. Unannealed samples exhibited essentially the same photocurrent densities for both substrates; however, it was evident that dark current densities for samples on FTO were higher than on titanium. This could have been due to different growth morphologies on the two substrates, giving a larger superficial area for FTO|Sn^{IV}-Fe_2O_3, or a higher electron energy barrier between Ti and Sn^{IV}-Fe_2O_3, caused by the growth of TiO_2 during annealing at 480 °C during the spray process. The latter phenomenon would also explain why after annealing Ti|Sn^{IV}-Fe_2O_3 samples, there is a significant decrease of dark current densities, yet no such change was detected with FTO|Sn^{IV}-Fe_2O_3. A thin layer of TiO_2 can grow during annealing at 400–500 °C, as demonstrated by Ong et al. [15]. If we compare the electron affinities (conduction band energies) of TiO_2, SnO_2 and α-Fe_2O_3: −4.21, −4.55 and −4.78 eV respectively on the physical scale [26], the electrons flowing from hematite to the substrate should tunnel through an energy barrier that is higher when a layer of TiO_2 is present. Tunnelling becomes inhibited with growth of > 1 nm of insulating TiO_2 [15,37], as will be seen below for different temperatures and times of annealing.

After treatment at 500 °C for 1 hour, there was a known shift of photocurrent onset to lower electrode potentials and a significant decrease in the maximum photocurrent densities [11]. Annealed samples of FTO|Sn^{IV}-Fe_2O_3 exhibited slightly lower photocurrent densities, but the same onset compared to Ti|Sn^{IV}-Fe_2O_3.

Fig. 2 shows the surface charge transfer efficiencies, $\eta_{surface}$, obtained from PEIS. Annealed samples showed a shift in photocurrent onset to lower potentials, which agrees with voltammograms shown in Fig. 1. The effect of the substrate was not evident in this case. Annealed samples on FTO and Ti exhibited identical behaviour.

As annealed Ti|Sn^{IV}-Fe_2O_3 samples exhibited greater photocurrent densities compared to FTO-supported samples, and considering that the use of FTO for large scale electrodes is not suitable due to the lower conductivity [12,15] and fragility, the present research focused mainly on the effect of post-annealing on photoelectrochemical properties of samples deposited on titanium. However, the use of 'bare' titanium as a substrate for thin films comes with challenges, such as constrained annealing temperatures to minimise rates of oxidation in air. Temperatures higher than 600 °C increase growth rates of TiO_2 significantly [16,38] and ultimately affect the performance of the photo-anodes due to the properties of TiO_2.

4.3. Annealing effect

Ti|Sn^{IV}-Fe_2O_3 samples annealed under different conditions were assessed in the absence and presence of H_2O_2 as a sacrificial electron donor. Fig. 3 shows that photocurrent densities measured on annealed samples shifted to lower potentials and the maximum photocurrent densities decreased with temperature and annealing time. According to a previous report [11], the shift to lower potentials is attributed to surface chemistry and catalysis effects, while the maximum current is thought to be a function of film morphology. The purpose of this study was to test these hypotheses at annealing temperatures of 400–500 °C, considering the following variables: morphology, crystallinity, donor density, absorbance, surface and bulk recombination, oxygen vacancies and dopant distribution inside the hematite semiconductor. Then, the

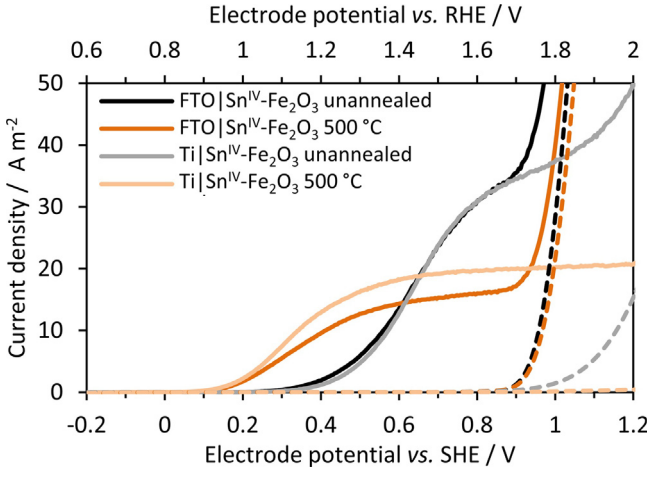

Fig. 1. Cyclic voltammograms of Sn^{IV}-doped α-Fe_2O_3 films deposited on FTO and Ti, without and with annealing at 500 °C for 60 min. A scan rate of 10 mV s^{-1}, 1 M NaOH electrolyte and irradiation of 3500 W m^{-2} by a Xe arc lamp were used. Dashed lines represent corresponding dark current densities.

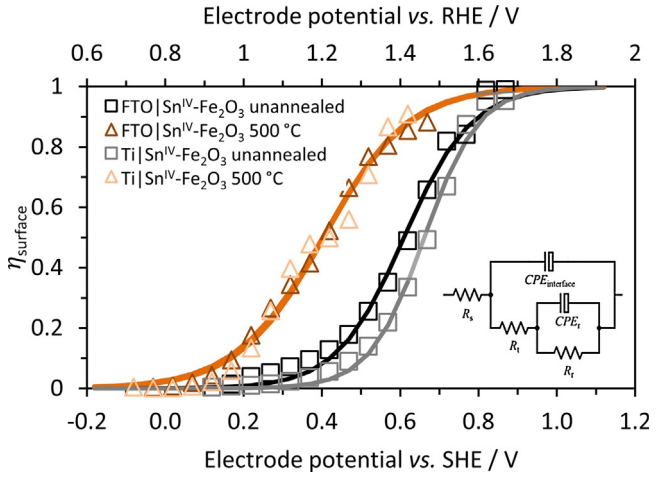

Fig. 2. Surface charge transfer efficiency of Sn^{IV}-doped α-Fe_2O_3 films deposited on FTO and Ti, unannealed and with annealing at 500 °C for 60 min. Calculated from fitting PEIS to the equivalent electrical circuit shown in the inset.

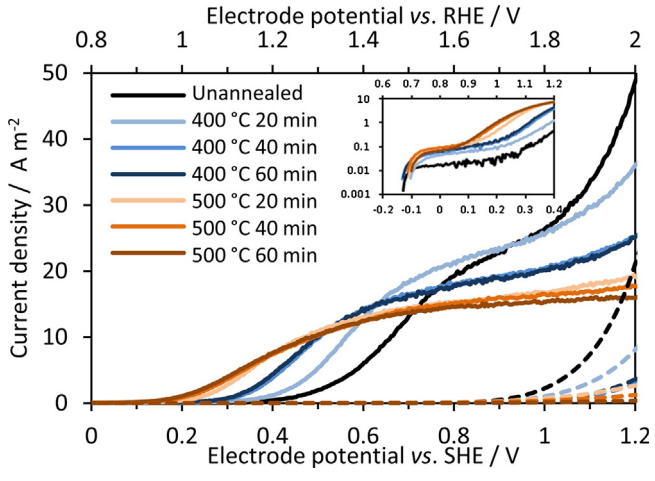

Fig. 3. Cyclic voltammograms on Ti|Sn^{IV}-doped α-Fe_2O_3 | 1 M NaOH at different annealing temperatures and times. A scan rate of 10 mV s^{-1}, and irradiation of 3000 W m^{-2} by a Xe arc lamp were used. Inset figure shows current densities on log scale. Dashed lines represent dark currents.

changes of these parameters were measured as a function of annealing temperature and time in order to explain the voltammetric behaviour shown in Fig. 3.

From the inset in Fig. 3, the onset potentials for all samples were very similar (ca. 0.7 V *vs.* RHE). It is also noteworthy that dark currents were highest for unannealed samples and decreased with annealing temperature and time. This could mean that morphological or catalytic changes happened on the surface of the photoelectrode or that an energy barrier was developed between hematite and titanium, as discussed previously.

Fig. 4 shows the effects of adding 0.5 M H_2O_2 as a hole scavenger to the electrolyte solution on voltammograms of photo-anode samples, thereby minimising electron-hole recombination rates. The onset potential (also ca. 0.7 V *vs.* RHE) was the same for all samples; only the maximum photocurrent density changed after annealing and followed the same trend found in the absence of H_2O_2. Dark current densities were again greater for the unannealed samples and decreased with increasing temperature and time of annealing. Thus, it can be concluded that the shift of photocurrent

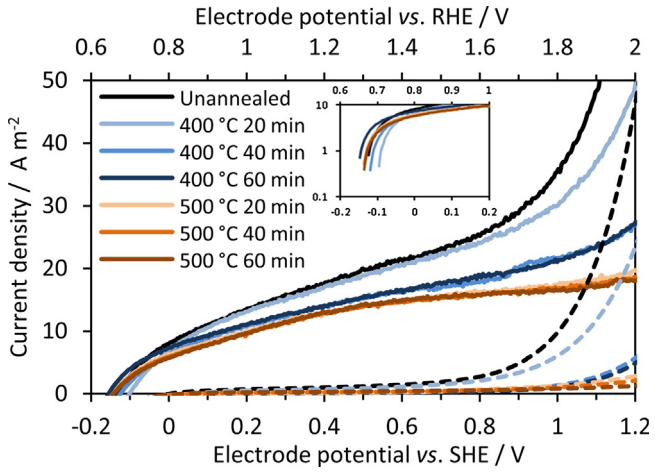

Fig. 4. Cyclic voltammograms of Ti|Sn^{IV}-doped α-Fe_2O_3 | 1 M NaOH + 0.5 M H_2O_2 for different annealing temperatures and times. A scan rate of 10 mV s^{-1}, and irradiation of 3000 W m^{-2} by a Xe arc lamp were used. Inset figure shows current densities on log scale. Dashed lines represent dark currents.

densities to lower potentials was due to peroxide ions minimising rates of surface recombination of electrons and holes; maximum photocurrent densities were not affected. This will be discussed further with PEIS measurements.

4.4. Incident photon-to-current efficiencies (IPCE)

IPCEs were evaluated under steady state conditions at two potentials: 1.51 V (Fig. 5a) and 1.71 V *vs.* RHE (Fig. 5b). At lower potentials, unannealed samples produced smaller photocurrent densities than heat-treated samples; this is in agreement with voltammograms shown in Fig. 1 and Fig. 3. At higher potentials and lower wavelengths, the IPCE values were similar for all samples. Remarkably, a shoulder at 550 nm was observed for unannealed samples and decreased in magnitude with increased temperature and time of annealing. This trend was also observed at 1.51 V *vs.* RHE after normalizing IPCEs with respect to the highest efficiency at 360 nm, shown in the supporting information, Fig. S3. This feature in IPCEs was also evident in samples deposited on FTO, so was not due to light being reflected from titanium substrates (see also Fig. S3).

IPCE values were integrated to estimate total current densities, as shown in detail in the supporting information, Fig. S4. The IPCE-estimated and measured photocurrent densities from cyclic voltammograms at 10 mV s^{-1} were very similar and supported the hypothesis that the difference in maximum photocurrent densities were related to the peak IPCE at 550 nm. This could have been due to a higher absorbance around that particular wavelength, a difference in crystallinity, different phase or redistribution of dopants in the semiconductor [35]. As the maximum photocurrent was mainly affected by the peak at 550 nm at 1.71 *vs.* RHE, catalytic and morphological changes were disregarded.

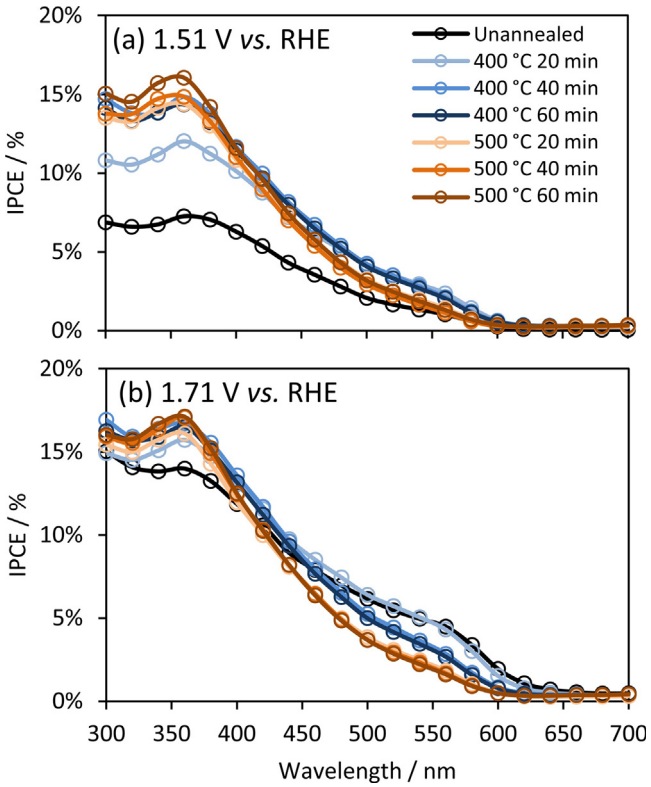

Fig. 5. IPCE spectra for Ti|Sn^{IV}-doped α-Fe_2O_3 | 1 M NaOH at (a) 1.51 and (b) 1.71 V *vs.* RHE.

4.5. Efficiencies of interfacial charge transfer

Efficiencies of interfacial charge transfer were studied further using the method proposed by Peter et al. [29,30] together with an equivalent circuit with two time constants to fit the PEIS spectra, as proposed by Klahr et al. [35]. Fig. 6 shows the experimental interfacial charge transfer efficiencies and fitted data for all samples. The shape is very similar to that evident from voltammograms in Fig. 3. However, such trends do not reflect the performance of the samples in terms of the maximum photocurrent densities, which were determined by other factors as discussed above. Again, the shape and shifting of the photocurrent curve to lower potentials was confirmed by the improvement of interfacial charge transfer efficiency due to less electron-hole recombination at the electrode | electrolyte interface.

4.6. Mott-Schottky analysis

Fig. 7 shows the Mott-Schottky plots under dark condition, generated using semiconductor capacitance values extracted from impedance data. The MS plots confirmed *n*-type behaviour of all samples and exhibited linear gradients; flat band potentials were estimated from intercepts with the potential axis. The data also showed a noticeable increase in gradients for annealed samples. Fig. 8 reports estimated donor densities, calculated using a relative permittivity of 38.2 ± 0.46 and a thickness of 47 ± 6 nm. After annealing, donor density values decreased by two orders of magnitude. Such high values could be explained by adventitious chloride on hematite surfaces residual from $FeCl_3$ used in its spray pyrolysis.

XPS confirmed the presence of a small amount of around 2 rel. at% of Cl compared to Fe on the film surface and subsequent disappearance after annealing on both FTO and titanium substrates; see Fig. S5 in supporting information. Oxygen vacancies, expressed as Fe^{2+}, could also have contributed to the difference between unannealed and annealed samples, and unusually high donor density (c.f. 1.98×10^{28} molecules Fe_2O_3 m^{-3}). However, XPS shows a Fe 2*p* line shape characteristic of α-Fe_2O_3 and no change in the binding energy at 716 eV, which is associated with the presence of oxygen vacancies close to the surface [39], see Fig. 12(a) in the XPS analysis section.

Additionally, the activation energy and diffusion coefficients for oxygen and iron self-diffusion were extrapolated from Amami et al. [40] to lower temperatures, in order to assess the possibility of formation or reduction of oxygen vacancies post-annealing. Diffusion coefficients accounting for oxygen inclusion and

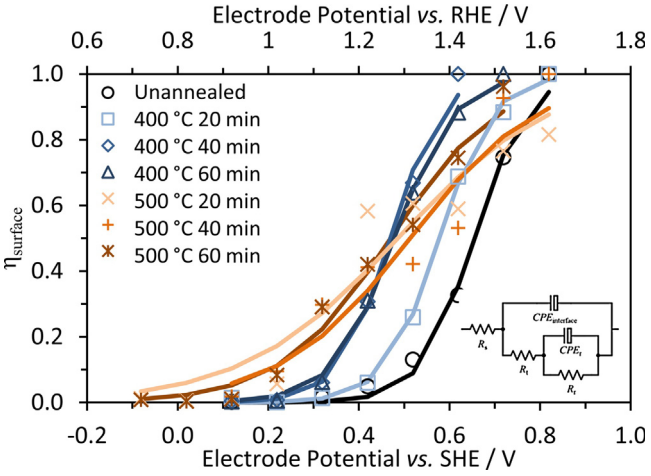

Fig. 6. Effects of potential and annealing temperature and time on interfacial charge transfer efficiencies for Ti|Sn^{IV}-doped α-Fe_2O_3 | 1 M NaOH, together with corresponding fitting to eq (6). Resistances were extracted from equivalent electric circuit shown in the inset.

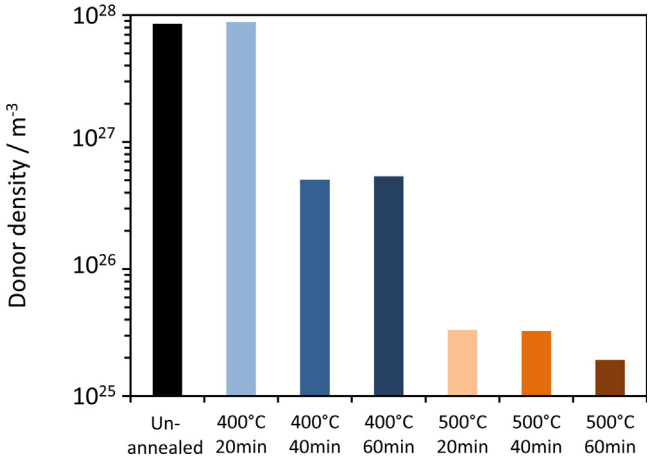

Fig. 8. Effects of annealing temperature and time on estimated donor densities from Mott-Schottky plots for Ti|Sn^{IV}-doped α-Fe_2O_3 | 1 M NaOH.

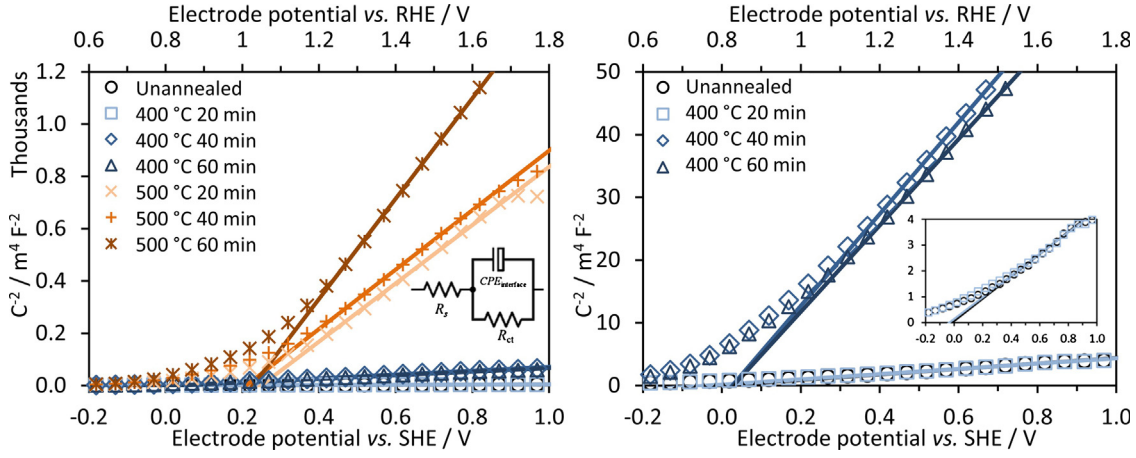

Fig. 7. Effects of annealing temperature and time on Mott-Schottky plots on Ti|Sn^{IV}-doped α-Fe_2O_3 | 1 M NaOH. Capacitances were extracted after fitting to a Randles circuit as shown in the inset.

exchange rate at the surface are of the order of 10^{-38} to $10^{-33}\,m^2\,s^{-1}$ for 400 and 500 °C, respectively, while diffusion coefficients accounting only for migration are of the order of $10^{-19}\,m^2\,s^{-1}$. Evidently, at such low temperatures, the fastest process is diffusion of oxygen and oxygen vacancies within the semiconductor bulk. Hence, rates of formation and exchange of oxygen vacancies at the surface is very low, so can be disregarded, as shown by XPS analysis.

Other possible reasons for such high donor densities and their decrease after annealing could be the existence of pinholes or changes in the Sn^{IV}-doped α-Fe_2O_3 | 1 M NaOH interfacial area; e.g. a change in the morphology could decrease the exposure of the substrate as a result of sintering. However, the morphology and topography of the samples on Ti and FTO, as shown later by SEM and AFM measurements, showed no substantial change with annealing.

It is worth mentioning that decoupling the relative permittivity and donor density ($\varepsilon_r n_0$) from Mott-Schottky relationship, eq (3), is experimentally challenging. Hence, there is a wide range of relative permittivity (25 – 120) [36,41–43] and donor density[27] values reported for hematite. Estimated donor densities of annealed and chloride free Sn^{IV}-doped α-Fe_2O_3 samples are between 3.3×10^{25} and $1.9\times10^{25}\,m^{-3}$. These values are in agreement with previous studies for Sn-doped hematite [14,22,36,42].

4.7. Flat band potential

The flat band potential of all samples was estimated using several methods, including MS analysis. Although the linear trends in C_{SC}^{-2}, shown in Fig. 7, appear reliable for the determination of flat band potential, the resulting values should be treated cautiously. Assumptions involved in MS analysis such as perfect smoothness of electrode surfaces (roughness factor of ca. 1) were invalid, as evident from the AFM reported below in Fig. 11. Values found with the Gärtner-Butler method (extrapolation of the linear portion of squared-photocurrent vs potential) and open circuit potential with high-intensity light [31], reported in Table 1, are very consistent and match with flat band constraints presented by Hankin et al. [27]. There was no clear trend for the reported values with temperature, so it can be assumed that low temperature annealing did not affect the flat band potential of Sn^{IV}-doped α-Fe_2O_3 significantly. The effect of changes in the flat band potential has also been discussed previously [27,31]. However, difficulties of measuring and constraints when using MS analysis make its estimation difficult. For hematite samples, squared-photocurrent in the presence of a hole scavenger (0.5 M H_2O_2) and under illumination with high light intensity appears to be a more practical and accurate method for quantifying this property as seen in Fig. S6 in the supporting information.

4.8. Photo-electrochemical impedance spectroscopy

The impedance under high-intensity light was measured at different potentials. Fig. 9 shows two different scenarios under biased conditions. When the electrode was operating at 1.21 V *vs.* RHE, a process at 1 Hz can be seen, which is completely absent at 1.71 V *vs.* RHE. This process is related to surface electron-hole recombination [35]. A second process at high frequencies was always present and was shifted to higher frequencies with time and temperature of annealing. This shift is associated with the decrease of interfacial capacitance, $C_{interface}$, which is actually the same as seen in MS analysis. The disappearance of the low frequency process is in agreement with the cyclic voltammograms, where at low potentials the surface recombination was predominant for unannealed samples. It is also evident from the bode plot at 1.21 *vs.* RHE that treated samples exhibited lower overall resistance, i.e. low frequency modulus, which is also in agreement with the reported cyclic voltammograms. This means that at that particular potential, surface recombination contributes significantly to the total impedance. On the other hand, at higher potentials (e.g. 1.71 V *vs.* RHE), the surface recombination process was supressed in all cases, but the low frequency modulus behaves

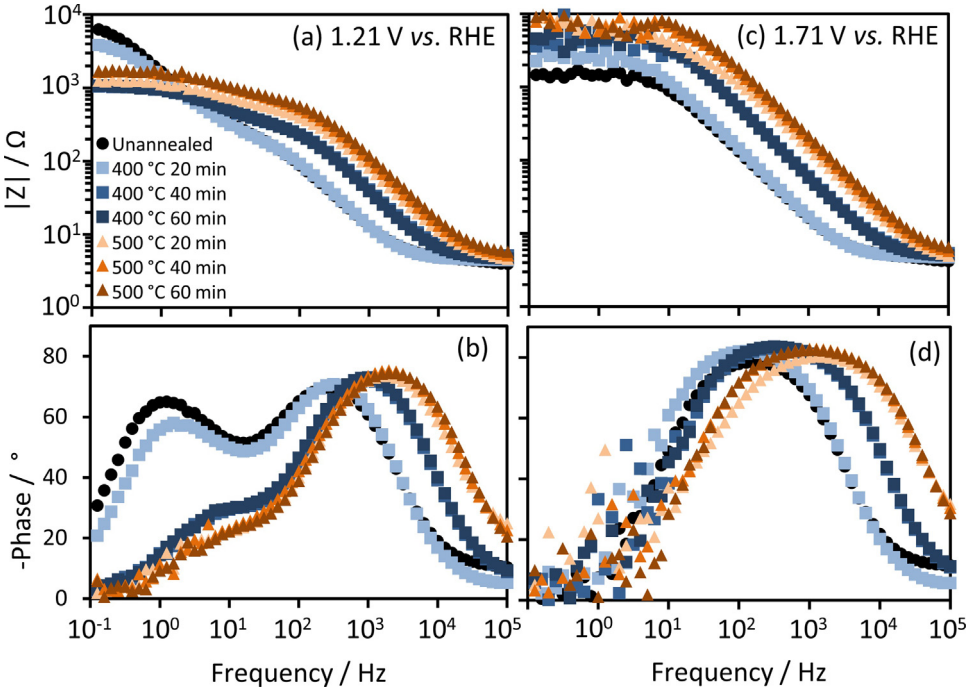

Fig. 9. Effect of annealing temperature and time on impedance spectra: 1.21 V *vs.* RHE (a) Bode and (b) phase plot, and 1.71 V *vs.* RHE (c) Bode and (d) phase plot of Ti|Sn^{IV}-doped α-Fe_2O_3 | 1 M NaOH under 3000 W m^{-2} Xe arc lamp.

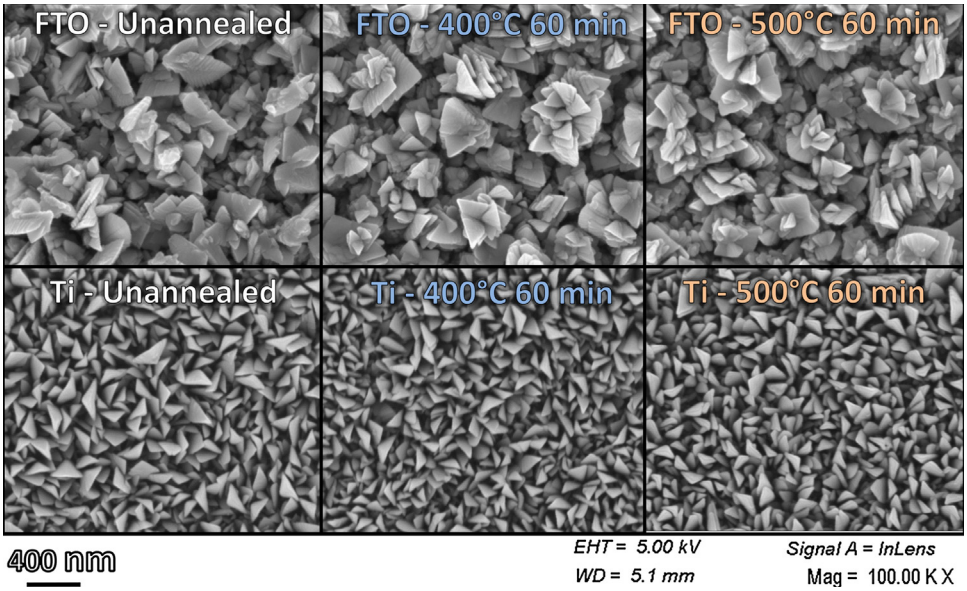

Fig. 10. SEM images (100k ×) of Sn^{IV}-doped α-Fe_2O_3 deposited on FTO and Ti, unannealed and annealed at 400 °C and 500 °C for 60 min.

in the opposite way. Unannealed samples exhibit lower resistance, which is in agreement again with previous voltammograms for unannealed samples (see Figs. 3 and 4).

In order to elucidate this point further, the phase from the impedance spectra was plotted in a heat map against potential and frequency for three samples: unannealed and annealed samples at 400 and 500 °C for 60 min (supporting information, Fig. S7). The process at 1 Hz related to surface recombination became weaker with annealing at higher potentials, while the charge transfer process became predominant and slightly shifted to higher frequencies with heat treatment.

4.9. Morphology and optical properties

The crystallinity of the samples was evaluated for the two extremes investigated in this study: unannealed samples and those

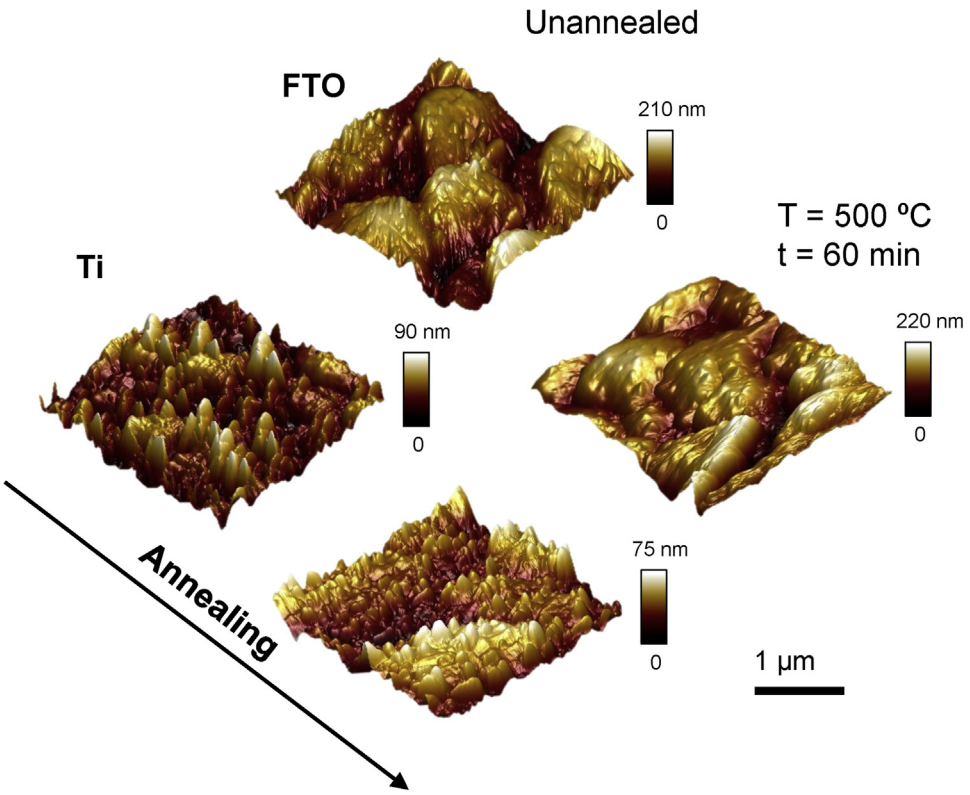

Fig. 11. AFM images of Sn^{IV}-doped α-Fe_2O_3 deposited on FTO and Ti, unannealed, 400 °C and 500 °C annealing for 60 minutes.

annealed at 500 °C for 60 min. Raman spectra, presented in the supporting information, Fig. S8, confirmed that the crystallinity of the samples did not change with annealing at temperatures up to 500 °C, and no other phases were evident in the film according to the expected peaks of hematite and TiO_2 phases, anatase and rutile, Table S1 [44–46]. A weak peak at 654 cm^{-1} could be associated with high density of defects in doped samples [47]. SEM images of Sn^{IV}-doped Fe_2O_3 deposited on FTO and Ti, Fig. 10, confirmed the nano-structured nature of the samples and also the independence of the morphology from annealing temperature (< 500 °C), which is also in agreement with previous findings of annealing at low temperatures [39,47]. Morphological changes with thermal treatment have been reported previously, but only for temperatures higher than 600 °C and longer exposures times [48].

Fig. 11 shows AFM images of the surface topography of Sn^{IV}-doped α-Fe_2O_3 on FTO and Ti substrates. Only a slight decrease in active area (< 11.6 % for FTO and < 7.6% for Ti samples) and roughness was evident after annealing, as reported in Table S2 in the supporting information. The increase of total active area with respect to the projected area was ca. 15% for samples deposited on FTO and 10% on Ti, in agreement with the SEM images. The AFM images also support the hypothesis that the unusually high values of donor density, via eq (3), and their substantial decrease with annealing were not associated with drastic changes in electroactive area, so were likely to be related to chloride contamination.

The absorbances of the various photo-anodes were measured to determine if the increase in IPCEs at 550 nm and 1.71 V *vs.* RHE was related to differences in absorbance at this wavelength. Samples treated at 500 °C showed higher absorbances in the UV region, consistent with a higher IPCE at 360 nm after annealing. However, there was no significant change in absorbance at 550 nm, as shown in the supporting information Fig. S9. Annealing at higher temperatures has been reported to affect the absorbance of samples significantly [48], but this was not evident for the 400–500 °C temperature range used in this work. No differences in band gaps were found from Tauc plots, shown in Fig. S10. Thus again, it can be concluded that the decrease of maximum photocurrent density with annealing at low temperatures was not related to changes in absorbance, crystallinity or morphology of the samples.

4.10. XPS Analysis

As the remaining hypothesis, the change in the maximum photocurrent and arrest at 550 nm in the IPCE could be related to a redistribution of the dopant. This is supported by a slight increase in the intensity of Sn 3*d* relative to Fe 2*p* core lines in the XPS spectra after annealing, see Fig. 12(b). From the comparison of the peak areas of the Sn $3d_{5/2}$ and Fe $2p_{3/2}$ lines, the Fe:Sn surface ratios are 98.4:1.6 and 98.2:1.8 for the unannealed films on FTO and Ti, respectively, and 97.9:2.1 and 97.8:2.2 for films annealed at 500 °C for 60 minutes on FTO and Ti, respectively. Thermal treatment is known to redistribute defects in semiconductors at the surface, where defects are at their lowest energy [49]. This would explain the diffusion of Sn^{IV} from the bulk to the surface after annealing.

Uchiyama et al. found a strong dependence of the optical absorption of hematite in the presence of Sn^{IV}. A molar ratio of 0.9:0.1 Fe^{3+}: Sn^{4+} exhibited lower absorbance in the visible region compared to samples in the absence of Sn^{IV}. A molar ratio 0.75:0.25 decreased the absorbance substantially, especially between 500 and 600 nm. It has also been reported [22] that increasing Sn doping levels from 0.75 to 2% can increase the band gap from 2.12 to 2.2 eV, i.e. decrease the absorption to lower wavelengths.

Frydrych et al. reported a correlation of the concentration of Sn^{IV} and the height of the Sn 3*d* XPS peak for hematite samples [17]. Assuming that after annealing, Sn^{IV} was concentrated within the depletion layer of the semiconductor, as well as the effective

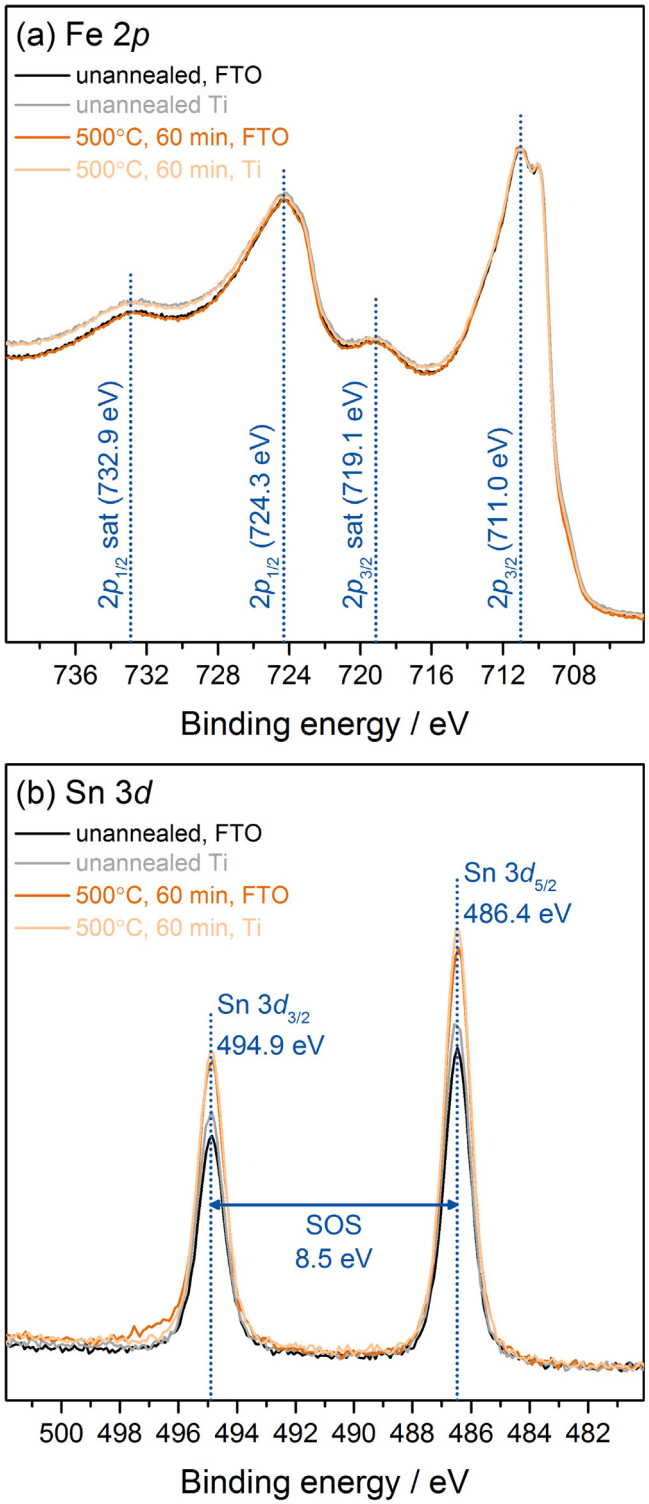

Fig. 12. XPS core level spectra of Sn^{IV}-doped α-Fe_2O_3 on FTO and titanium unannealed and after annealing at 500 °C for 60 minutes, including (a) Fe 2p and (b) Sn 3d.

electron-hole separation occurred in this region [18,20], the decrease of the IPCE peak at 550 nm could be explained by a corresponding decrease of photon absorption. However, this was not evident in the absorption spectra (Fig. S9), because photons between 500 and 600 nm would still be absorbed in the bulk of the photo-anode, but would not be converted effectively to charge due

Table 1
Effects of annealing temperature and time on flat band potential *vs.* RHE (V) for Ti|Sn^{IV}-doped α-Fe_2O_3 | 1 M NaOH estimated by different methods.

Sample	MS	OCP(photo) 1 M NaOH	OCP(photo) 1 M NaOH + 0.5 M H_2O_2	j^2_{ph}
Unannealed	0.77	0.71	0.68	0.71
400 °C 20 min	0.75	0.71	0.71	0.70
400 °C 40 min	0.80	0.67	0.69	0.70
400 °C 60 min	0.81	0.67	0.65	0.66
500 °C 20 min	1.03	0.71	0.67	0.69
500 °C 40 min	0.99	0.71	0.67	0.71
500 °C 60 min	1.01	0.73	0.67	0.72

to electron-hole recombination in the bulk hematite. Depletion of Sn^{IV} in the bulk of the semiconductor due to its diffusion to the surface could also have caused the decrease in maximum photocurrent on annealing. Sn^{IV} depletion in the bulk could increase the electron-hole recombination rates there and also alter the electrical conductivity [3]. Also, a decrease in the semiconductor Debye length due to higher concentrations of donors (Sn^{IV}) near the surface could result in a decrease in the number of absorbed photons in the depletion layer [22].

Sn^{IV}-doped α-Fe_2O_3 exhibited higher efficiencies of interfacial charge transfer compared to undoped samples [25]. The presence of higher Sn^{IV} concentrations close to the Sn^{IV}-doped α-Fe_2O_3 | 1 M NaOH interface increased photocurrent densities which were shifted to lower potentials, due to decreased surface electron-hole recombination rates and/or improved catalysis of the oxygen evolution reaction.

Profiling of dopant concentration inside Sn^{IV}-doped α-Fe_2O_3 is necessary to elucidate further the effects of annealing on the photo-electrochemical properties of hematite. This can be done via ion beam sputtering. However, Sn and Fe might sputter at different rates and also be reduced to elemental form, changing the stoichiometry and concentration of the sample [50,51]. Intensity modulated photo-electrochemical impedance spectroscopy (IMPS) and transient absorption spectroscopy (TAS) with 550 nm monochromatic light may also prove useful in elucidating the origin of this phenomenon.

5. Conclusions

Sn^{IV}-doped α-Fe_2O_3 photo-anodes were fabricated via spray pyrolysis on titanium and FTO substrates and the effects studied of subsequent annealing at 400 and 500 °C, at which spatial redistributions of Sn^{IV} was suggested to occur. The shift of photocurrent densities with annealing temperature in absence of hole scavenger was associated with a decrease of electron-hole recombination rates caused by an increase of dopant concentration near the Sn^{IV}-doped α-Fe_2O_3 | 1 M NaOH interface. No evidence was found for annealing causing significant changes in morphology, crystallinity or topography. The decrease in maximum photocurrent densities with annealing appeared to be associated with a decrease in photon absorption within the depletion layer where Sn^{IV} dopant was believed to have accumulated, with supporting evidence from IPCE spectra and XPS measurements. After excluding effects due to changes in morphology [11], which occurs only at higher temperatures, changes in photo-electrochemical behaviour after annealing were explained in terms of Sn^{IV} dopant concentration profiles, leading to decreased fluxes of holes [52].

A complete summary of all the phenomena and hypotheses investigated are listed in table S3 in the supporting information. The results and a clearer understanding of the effects of various parameters on photo-anode performance could serve as a framework to improve models to predict photocurrent densities in scaled-up photo-electrochemical reactors for hydrogen production [28].

Acknowledgments

The authors thank the UK Engineering and Physical Sciences Research Council for a post-doctoral research associateship for AH, COLCIENCIAS scholarship 568 for PhD studies abroad for FB, and also the help of Alessandra Vichi with Raman measurements.

Appendix A. Supplementary data

Supplementary data associated with this article can be found, in the online version, at http://dx.doi.org/10.1016/j.electacta.2017.08.090. Also, the underlying research data for this paper is available in accordance with EPSRC open data policy from https://zenodo.org/record/845452#.WZrdWz75hQI

References

[1] R. van de Krol, M. Grätzel, Photoelectrochemical Hydrogen Production, (2012).
[2] B. Iandolo, B. Wickman, I. Zoric, A. Hellman, The rise of hematite: origin and strategies to reduce the high onset potential for the oxygen evolution reaction, Journal of Materials Chemistry A 3 (2015) 16896–16912.
[3] Y. Ling, Y. Li, Review of Sn-Doped Hematite Nanostructures for Photoelectrochemical Water Splitting, Particle & Particle Systems Characterization 31 (2014) 1113–1121.
[4] S. Sahai, A. Ikram, S. Rai, S. Dass, R. Shrivastav, V.R. Satsangi, CdSe quantum dots sensitized nanoporous hematite for photoelectrochemical generation of hydrogen, International Journal of Hydrogen Energy 39 (2014) 11860–11866.
[5] L. Steier, J. Luo, M. Schreier, M.T. Mayer, T. Sajavaara, M. Grätzel, Low-Temperature Atomic Layer Deposition of Crystalline and Photoactive Ultrathin Hematite Films for Solar Water Splitting, ACS Nano 9 (2015) 11775–11783.
[6] O. Zandi, A.R. Schon, H. Hajibabaei, T.W. Hamann, Enhanced Charge Separation and Collection in High-Performance Electrodeposited Hematite Films, Chemistry of Materials 28 (2016) 765–771.
[7] J.Y. Kim, D.H. Youn, J.H. Kim, H.G. Kim, J.S. Lee, Nanostructure-Preserved Hematite Thin Film for Efficient Solar Water Splitting, ACS Applied Materials & Interfaces 7 (2015) 14123–14129.
[8] M. Forster, R.J. Potter, Y. Ling, Y. Yang, D.R. Klug, Y. Li, A.J. Cowan, Oxygen deficient [small alpha]-Fe_2O_3 photoelectrodes: a balance between enhanced electrical properties and trap-mediated losses, Chemical Science 6 (2015) 4009–4016.
[9] K. Schulz, R. Schmack, H.W. Klemm, A. Kabelitz, T. Schmidt, F. Emmerling, R. Kraehnert, Mechanism and Kinetics of Hematite Crystallization in Air: Linking Bulk and Surface Models via Mesoporous Films with Defined Nanostructure, Chemistry of Materials 29 (2017) 1724–1734.
[10] M. Li, J. Deng, A. Pu, P. Zhang, H. Zhang, J. Gao, Y. Hao, J. Zhong, X. Sun, Hydrogen-treated hematite nanostructures with low onset potential for highly efficient solar water oxidation, Journal of Materials Chemistry A 2 (2014) 6727–6733.
[11] K. Sivula, F. LeFormal, M. Grätzel, Solar Water Splitting: Progress Using Hematite (α-Fe_2O_3) Photoelectrodes, ChemSusChem 4 (2011) 432–449.
[12] C. Carver, Z. Ulissi, C.K. Ong, S. Dennison, G.H. Kelsall, K. Hellgardt, Modelling and development of photoelectrochemical reactor for H_2 production, International Journal of Hydrogen Energy 37 (2012) 2911–2923.
[13] K. Sivula, R. Zboril, F. Le Formal, R. Robert, A. Weidenkaff, J. Tucek, J. Frydrych, M. Grätzel, Photoelectrochemical Water Splitting with Mesoporous Hematite Prepared by a Solution-Based Colloidal Approach, Journal of the American Chemical Society 132 (2010) 7436–7444.
[14] Y. Ling, G. Wang, D.A. Wheeler, J.Z. Zhang, Y. Li, Sn-Doped Hematite Nanostructures for Photoelectrochemical Water Splitting, Nano Letters 11 (2011) 2119–2125.

[15] C.K. Ong, S. Dennison, S. Fearn, K. Hellgardt, G.H. Kelsall, Behaviour of Titanium-based Fe_2O_3 Photo-Anodes in Photo-Electrochemical Reactors for Water Splitting, Electrochimica Acta 125 (2014) 266–274.
[16] K.H.P. Kofstad, Investigation on the Oxidation Mechanism of Titanium, Acta Chemica Scandinavica 12 (1958) 239–266.
[17] J. Frydrych, L. Machala, J. Tucek, K. Siskova, J. Filip, J. Pechousek, K. Safarova, M. Vondracek, J.H. Seo, O. Schneeweiss, M. Gratzel, K. Sivula, R. Zboril, Facile fabrication of tin-doped hematite photoelectrodes – effect of doping on magnetic properties and performance for light-induced water splitting, Journal of Materials Chemistry 22 (2012) 23232–23239.
[18] P.S. Bassi, L. Xianglin, Y. Fang, J.S.C. Loo, J. Barber, L.H. Wong, Understanding charge transport in non-doped pristine and surface passivated hematite (Fe_2O_3) nanorods under front and backside illumination in the context of light induced water splitting, Physical Chemistry Chemical Physics 18 (2016) 30370–30378.
[19] R. Milan, S. Cattarin, N. Comisso, C. Baratto, K. Kaunisto, N.V. Tkachenko, I. Concina, Compact hematite buffer layer as a promoter of nanorod photoanode performances, Sci. Rep. 6 (2016) 35049.
[20] U. Bjoerksten, J. Moser, M. Graetzel, Photoelectrochemical Studies on Nanocrystalline Hematite Films, Chemistry of Materials 6 (1994) 858–863.
[21] C.K. Ong, S. Dennison, K. Hellgardt, G. Kelsall, Evaluation and Modeling of a Photo-Electrochemical Reactor for Hydrogen Production Operating under High Photon Flux, ECS Transactions 35 (2011) 11–19.
[22] V.M. Aroutiounian, V.M. Arakelyan, G.E. Shahnazaryan, H.R. Hovhannisyan, H. Wang, J.A. Turner, Photoelectrochemistry of tin-doped iron oxide electrodes, Solar Energy 81 (2007) 1369–1376.
[23] P. Dias, A. Vilanova, T. Lopes, L. Andrade, A. Mendes, Extremely stable bare hematite photoanode for solar water splitting, Nano Energy 23 (2016) 70–79.
[24] C.K. Ong, Design and Performance of Photo-electrochemical Reactors with Fe_2O_3 Photo-anodes for Water Splitting, Department of Chemical Engineering, Imperial College London, London, 2013.
[25] H.K. Dunn, J.M. Feckl, A. Muller, D. Fattakhova-Rohlfing, S.G. Morehead, J. Roos, L.M. Peter, C. Scheu, T. Bein, Tin doping speeds up hole transfer during light-driven water oxidation at hematite photoanodes, Physical Chemistry Chemical Physics 16 (2014) 24610–24620.
[26] Y. Xu, M.A.A. Schoonen, The absolute energy positions of conduction and valence bands of selected semiconducting minerals, American Mineralogist 85 (2000) 543–556.
[27] A. Hankin, J.C. Alexander, G.H. Kelsall, Constraints to the flat band potential of hematite photo-electrodes, Physical Chemistry Chemical Physics 16 (2014) 16176–16186.
[28] A. Hankin, F.E. Bedoya-Lora, C.K. Ong, J.C. Alexander, F. Petter, G.H. Kelsall, From millimetres to metres: the critical role of current density distributions in photo-electrochemical reactor design, Energy Environ. Sci. 10 (2017) 346–360.
[29] K.G. Upul Wijayantha, S. Saremi-Yarahmadi, L.M. Peter, Kinetics of oxygen evolution at Fe_2O_3 photoanodes: a study by photoelectrochemical impedance spectroscopy, Physical Chemistry Chemical Physics 13 (2011) 5264–5270.
[30] L.M. Peter, Energetics and kinetics of light-driven oxygen evolution at semiconductor electrodes: the example of hematite, J Solid State Electrochem 17 (2013) 315–326.
[31] W.P. Gomes, F. Cardon, Electron energy levels in semiconductor electrochemistry, Progress in Surface Science 12 (1982) 155–215.
[32] H.N.D. Zhebo Chen, Eric Miller, Photoelectrochemical Water Splitting Standards, Experimental Methods, and Protocols, Springer, 2013.
[33] Y. Ma, S.R. Pendlebury, A. Reynal, F. Le Formal, J.R. Durrant, Dynamics of photogenerated holes in undoped BiVO4 photoanodes for solar water oxidation, Chemical Science 5 (2014) 2964–2973.
[34] B. Hirschorn, M.E. Orazem, B. Tribollet, V. Vivier, I. Frateur, M. Musiani, Determination of effective capacitance and film thickness from constant-phase-element parameters, Electrochimica Acta 55 (2010) 6218–6227.
[35] B. Klahr, S. Gimenez, F. Fabregat-Santiago, T. Hamann, J. Bisquert, Water Oxidation at Hematite Photoelectrodes: The Role of Surface States, Journal of the American Chemical Society 134 (2012) 4294–4302.
[36] H. Uchiyama, M. Yukizawa, H. Kozuka, Photoelectrochemical Properties of Fe_2O_3-SnO_2 Films Prepared by Sol-Gel Method, The Journal of Physical Chemistry C 115 (2011) 7050–7055.
[37] S. Rühle, D. Cahen, Electron Tunneling at the TiO_2/Substrate Interface Can Determine Dye-Sensitized Solar Cell Performance, The Journal of Physical Chemistry B 108 (2004) 17946–17951.
[38] M.V. Diamanti, S. Codeluppi, A. Cordioli, M.P. Pedeferri, Effect of thermal oxidation on titanium oxides' characteristics, Journal of Experimental Nanoscience 4 (2009) 365–372.
[39] Y. Ling, G. Wang, J. Reddy, C. Wang, J.Z. Zhang, Y. Li, The Influence of Oxygen Content on the Thermal Activation of Hematite Nanowires, Angewandte Chemie International Edition 51 (2012) 4074–4079.
[40] B. Amami, M. Addou, F. Millot, A. Sabioni, C. Monty, Self-diffusion in α-Fe_2O_3 natural single crystals, Ionics 5 (1999) 358–370.
[41] I. Cesar, K. Sivula, A. Kay, R. Zboril, M. Grätzel, Influence of Feature Size, Film Thickness, and Silicon Doping on the Performance of Nanostructured Hematite Photoanodes for Solar Water Splitting, The Journal of Physical Chemistry C 113 (2009) 772–782.
[42] F.A. Benko, J. Longo, F.P. Koffyberg, A Comparison of Photochemical Properties of Amorphous and Polycrystalline Fe_2O_3, Journal of The Electrochemical Society 132 (1985) 609–613.
[43] R.A. Lunt, A.J. Jackson, A. Walsh, Dielectric response of Fe_2O_3 crystals and thin films, Chemical Physics Letters 586 (2013) 67–69.
[44] D.L.A. de Faria, S. Venâncio Silva, M.T. de Oliveira, Raman microspectroscopy of some iron oxides and oxyhydroxides, Journal of Raman Spectroscopy 28 (1997) 873–878.
[45] T. Ohsaka, F. Izumi, Y. Fujiki, Raman spectrum of anatase, TiO2, Journal of Raman Spectroscopy 7 (1978) 321–324.
[46] S.P.S. Porto, P.A. Fleury, T.C. Damen, Raman Spectra of TiO_2, MgF_2 ZnF_2 FeF_2, and MnF_2, Physical Review 154 (1967) 522–526.
[47] X. Yang, R. Liu, Y. Lei, P. Li, K. Wang, Z. Zheng, D. Wang, Dual Influence of Reduction Annealing on Diffused Hematite/FTO Junction for Enhanced Photoelectrochemical Water Oxidation, ACS Applied Materials & Interfaces 8 (2016) 16476–16485.
[48] R. Morrish, M. Rahman, J.M.D. MacElroy, C.A. Wolden, Activation of Hematite Nanorod Arrays for Photoelectrochemical Water Splitting, ChemSusChem 4 (2011) 474–479.
[49] R.B. Beall, J.B. Clegg, J.J. Harris, Migration of Si in δ-doped GaAs, Semiconductor Science and Technology 3 (1988) 612.
[50] D. Briggs, M.P. Seah, Practical Surface Analysis, Auger and X-ray Photoelectron Spectroscopy, Wiley, 1990.
[51] B.V. King, I.S.T. Tsong, The depth resolution of sputter profiling, Ultramicroscopy 14 (1984) 75–78.
[52] M.J. Katz, S.C. Riha, N.C. Jeong, A.B.F. Martinson, O.K. Farha, J.T. Hupp, Toward solar fuels: Water splitting with sunlight and rust? Coordination Chemistry Reviews 256 (2012) 2521–2529.